Activity Descriptor Identification for Oxygen Reduction on Platinum-Based Bimetallic Nanoparticles: *In Situ* Observation of the Linear Composition–Strain–Activity Relationship

Qingying Jia,[†] Wentao Liang,[‡] Michael K. Bates,[†] Prasanna Mani,[§] Wendy Lee,[§] and Sanjeev Mukerjee*[,†]

[†]Department of Chemistry and Chemical Biology and [‡]Department of Biology, Northeastern University, Boston, Massachusetts 02115, United States and [§]Automotive Fuel Cell Cooperation Corporation, Burnaby, British Columbia V5J 5J8, Canada

ABSTRACT Despite recent progress in developing active and durable oxygen reduction catalysts with reduced Pt content, lack of elegant bottom-up synthesis procedures with knowledge over the control of atomic arrangement and morphology of the Pt–alloy catalysts still hinders fuel cell commercialization. To follow a less empirical synthesis path for improved Pt-based catalysts, it is essential to correlate catalytic performance to properties that can be easily controlled and measured experimentally. Herein, using Pt–Co alloy nanoparticles (NPs) with varying atomic composition as an example, we show that the atomic distribution of Pt-based bimetallic NPs under operating conditions is strongly dependent on the initial atomic ratio by employing microscopic and *in situ* spectroscopic techniques. The Pt_xCo/C NPs with high Co content possess a Co concentration gradient such that Co is concentrated in the core and gradually depletes in the near-surface region, whereas the Pt_xCo/C NPs with low Co content possess a relatively uniform distribution of Co with low Co population in the near-surface region. Despite their different atomic structure, the oxygen reduction reaction (ORR) activity of Pt_xCo/C and Pt/C NPs is linearly related to the bulk average Pt–Pt bond length (R_{Pt-Pt}). The R_{Pt-Pt} is further shown to contract linearly with the increase in Co/Pt composition. These linear correlations together demonstrate that (i) the improved ORR activity of Pt_xCo/C NPs over pure Pt NPs originates predominantly from the compressive strain and (ii) the R_{Pt-Pt} is a valid strain descriptor that bridges the activity and atomic composition of Pt-based bimetallic NPs.

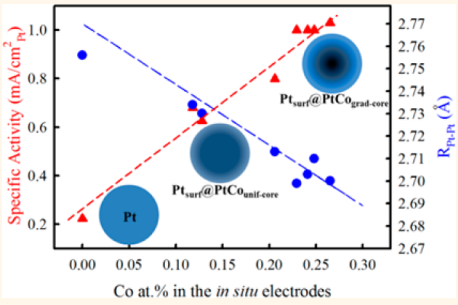

KEYWORDS: oxygen reduction reaction · Pt-bimetallic nanoparticles · X-ray absorption spectroscopy · strain effects · activity descriptor

Extensive efforts have been dedicated to the development of polymer electrolyte membrane fuel cells (PEMFCs) as promising alternatives to fossil fuels owing to their high energy efficiency and low emissions.[1−3] The main bottlenecks for PEMFC technology are the sluggish oxygen reduction reaction (ORR) and the high cost of platinum required to accelerate the ORR in the highly acidic and oxidizing environment of a PEMFC cathode.[4−6] The development of active and durable catalysts with reduced Pt content is of paramount importance for PEMFC commercialization. Much progress has been made in reducing the Pt loading by alloying Pt with transition metals such as Co, Ni, Cu, *etc.*, as not only is less Pt wasted in the core, but the Pt-based alloys (PtM) often exhibit enhanced activity and durability compared to pure Pt.[7−11] The promoting effects induced by the transition metal are to weaken the binding energies of oxygen-containing ORR intermediates (*e.g.*, O, OH, OOH) *via* altering the electronic property (such as the d-band center or vacancy) of the Pt-rich shell.[12−15] This is primarily induced by two effects: the geometric or the strain effects that refer to the changes in the Pt–Pt bond distance on the surface,[16−18] and the electronic or

* Address correspondence to s.mukerjee@neu.edu.

Received for review September 26, 2014 and accepted January 5, 2015.

Published online January 05, 2015
10.1021/nn506721f

the ligand effects that refer to the heterometallic bonding interactions between the Pt surface and the alloy substrate.[17−20] These two effects can be fully accounted for by the d-band theory developed by Nørskov *et al.*,[12,14,17,21] which demonstrates that the Pt surface d-band center (with some limitations[22]) or the Pt−O binding energy can serve as a valid activity descriptor for Pt-based catalysts with well-characterized surfaces. However, it is impractical to use these properties as activity descriptors for PtM NPs given the fact that they can be measured only on well-characterized surfaces in ultrahigh vacuum (UHV), whereas the surface composition and morphology of PtM NPs are complicated and often change drastically under the electrochemical environment during reactions. Although the beneficial role of M in the ORR activity of PtM NP catalysts is generally understood, a clear correlation between their ORR activity and atomic structure has not been established. Neither has a valid activity descriptor that can be easily controlled and measured been identified. This causes the catalyst synthetic approaches to be more empirical with little knowledge on the structural and morphological factors to be controlled in order to achieve the most optimal catalyst structure with highest activity.

The atomic composition plays a critical role in determining the particle morphology and ORR activity of PtM NPs. Pt mass-based activity (MA) enhancements of a factor of 1.5−2.5 compared to Pt/C NPs have been reported in conventional Pt_xM ($x > 1$) NPs.[7,8,23,24] More recently, M-rich Pt_xM NPs ($x \leq 1$) subjected to an (electro)chemical dealloying process in acid are demonstrated to exhibit 4−8 times higher MA than the state-of-the-art Pt/C,[9,25−28] superior to those of conventional Pt alloys. The conventional and newly developed dealloyed PtM catalysts possess dissimilar structures, which to a large extent arises from their different precursor atomic compositions. In general, the depletion of the soluble transition metal M in Pt_xM alloys with low M concentration ($x > 1$) in acidic pH environment is limited to the surface region, resulting in thin Pt-rich shell and solid M-rich core structures. In the case of Pt_xM NPs with high M concentration ($x \leq 1$), the depletion of soluble transition metal penetrates into the inner core, leading to thick Pt-rich shell and porous M-rich core structures.[29,30] The different levels of enhancement in ORR activity of these Pt_xM alloys relative to Pt/C have thus been ascribed to their dissimilar compositions and structures. Specifically, the enhanced ORR activities of the conventional Pt_xM ($x \geq 1$) catalysts were attributed to the convoluted strain and ligand effects as suggested by the contracted Pt−Pt bond distance and altered Pt d-electron vacancy observed by X-ray absorption spectroscopy (XAS).[7,8,23] On the other hand, the high activity of the dealloyed Pt_xM ($x \leq 1$) is predominantly ascribed to the strong strain effects induced by the high M content in the core.[31] The ligand effects, which decay rapidly with layer thickness,[19] are negligible owing to the thick Pt overlayers. Strasser *et al.*[31] further show that the specific activity (SA) of dealloyed Pt_xCu NPs increases with the Cu content in the as-synthesized catalysts owing to the increasing strain. In a more recent work, they refined their earlier reports by claiming monotonic relations between the ORR activity of Pt−Ni alloy NPs with similar particle size and the initial Ni content and identifying the initial Ni content as a good descriptor for ORR activity.[32]

However, the initial M content in the as-synthesized PtM NP catalysts can vary significantly from the residual M content in the *in situ* electrodes since a great deal of M (a less noble metal) is preferentially dissolved during the (electro)chemical dealloying, the cyclic voltammetric pretreatment, and/or the PEMFC operation.[31−34] As both strain and ligand effects are induced by the M atoms in the PtM NPs under operation, it is intuitive to employ the Pt/M ratio in the *in situ* electrodes rather than in the as-synthesized powders to truly understand the composition effects on the ORR activity of PtM NPs. Indeed, it was recently shown that ORR activity of an as-synthesized $PtNi_3$/C NP catalyst subjected to the chemical dealloying process with varying gas environments and acids varies significantly despite the identical initial Ni content and tracks well with the residual Ni content.[35−37] On the other hand, we found the ORR activities of the Pt_1Co_1/C and Pt_1Co_3/C NP catalysts undergoing the same dealloying and preparation process were essentially the same despite the different initial Co content, which may be related to their comparable residual Co content.[33,38] The monotonic relation between the ORR activity of Pt−Ni alloy NPs and the initial Ni content uncovered by Strasser *et al.*[32] is likely due to the monotonic relation between the initial and residual Ni content of this type of catalyst. However, in general the initial and residual M content is not monotonically correlated, as the extent of M loss varies significantly depending on the initial Pt/M atomic ratio in the as-synthesized catalysts as aforementioned. For instance, multiple groups found that the as-synthesized $PtCo_3$ NP catalyst ends up with a similar or even lower Co content than the as-synthesized Pt_1Co_1 NP catalyst after the electrochemical treatments in acid.[29,33,38] However, the intrinsic correlation between the ORR activity of PtM NP catalysts and their residual M content has not been established so far, and neither has a valid structural descriptor been identified that bridges the activity and the residual M content to reveal the physical origin of the composition−activity correlation.

Another pathway to increase the ORR activity of PtM NPs is to increase the atomic distribution (or alloying extent). Hwang *et al.*[39] proposed that the Pt_xCo NPs with higher atomic distribution exhibit better ORR activity since the promoted electron transfer from Co

TABLE 1. Summary of Element Analysis, XRD, and TEM Results

catalyst	Pt (wt %)	Co (wt %)	Pt:Co (atomic ratio)	lattice parameter (Å)	crystallite size (nm)	particle size[a] (nm)
Pt_2Co/C	47.0	6.9	2.1	3.79	4.0	4.3 ± 1.1
Pt_3Co/C	28.8	3.1	2.8	3.83	3.3	3.9 ± 0.9
Pt_4Co/C	31.4	2.3	4.1	3.84	3.2	4.3 ± 0.6
Pt_6Co/C	49.9	2.4	6.3	3.87	4.9	5.0 ± 1.0
Pt_7Co/C	30.1	1.3	7.0	3.88	3.9	3.9 ± 0.7
Pt/C	52.5			3.92	4.7	4.8 ± 1.2

[a] At least 100 particles were collected for particle size estimation. The ± indicates standard deviation.

to Pt creates fewer unoccupied d-orbitals of Pt. In addition, Shao-Horn *et al.*[40] found that the ORR specific activity of the acid-leached "Pt_3Co" catalyst can be further increased by annealing it at high temperature, which forms a so-called "sandwich" structure by driving some Co atoms from the core to the subsurface. The enriched Co in the near-surface region, with consequent increase of Co atomic distribution, not only induces ligand effects but also compresses the surface Pt−Pt bond distance by suppressing the outward surface relaxation.[41,42] However, the atomic structure of PtM NPs often changes under *in situ* electrochemical reaction conditions.[43,44] For instance, it was reported that the atomic structure of $PtNi_6/C$ NPs transforms from chemically disordered nanophases to ordered alloy nanophases during electrochemical activation cycling, accompanied by a substantial increase in the catalytic activity,[44] whereas the ordered nanophases of Pt−Co/C NPs may change to disordered ones under electrochemical treatment.[45] Therefore, it is crucial to identify the atomic distribution of PtM NPs under *in situ* ORR conditions as well.

In this context, we have systematically conducted *ex situ* microscopic and *in situ* XAS studies on a series of Pt_xCo/C NPs with varying precursor composition. The goal of this work is to develop an in-depth understanding of the relationships between the composition−structure and structure−activity of Pt-based bimetallic NPs under *in situ* electrochemical conditions and to seek valid descriptors of their ORR activity. The bond distance, atomic composition, and atomic distribution of the NPs under ORR operating conditions, properties that are the most relevant for determining the critical bulk morphology of bimetallic NPs, were quantitatively determined by a comprehensive EXAFS (extended X-ray absorption fine structure) analysis. The surface morphology and the oxygenated adsorbate coverage as a function of applied potential were obtained by surface-sensitive $\Delta\mu$-XANES (X-ray absorption near-edge structure) analysis. These, along with the electrochemical measurements (cyclic voltammetry and rotating ring disk electrode), provide unique valuable information about the relationship between atomic structure and ORR activity, which is not accessible from *ex situ* experimental measurements. We thereby established a quantitative composition−strain−activity correlation of Pt_xCo/C NP catalysts and identified valid ORR activity descriptors that can be measured experimentally and easily controlled. The findings from this work along with the approach used to identify the detailed atomic structure under *in situ* operating conditions are applicable to a broad range of bimetallic NP catalysts as well, providing a fundamental understanding of the atomic factors governing their catalytic activity.

RESULTS

***Ex Situ* Characterizations.** Table 1 summarizes the *ex situ* characterization results of the as-received Pt_xCo/C and Pt/C NPs including Pt and Co weight percentage and the nominal atomic composition obtained by the element analysis conducted by TKK Inc., the crystallite size and the lattice parameter given by XRD, and the particle size distribution revealed by TEM. Note the atomic composition and distribution of the as-received samples could vary significantly under *in situ* working conditions, as emphasized in the introduction part. In the text and figure captions we refer to the samples according to their nominal atomic ratio unless mentioned otherwise. Scanning electron microscopy (SEM) shows (Figure S1) that the nanoparticles are well dispersed on the highly porous carbon surface. The Pt/Co atomic compositions obtained by energy dispersive X-ray spectroscopy (EDS) match those provided by TKK Inc. Transmission electron microscopy (TEM) (Figure S2) shows that all the catalysts possess comparable mean particle sizes (∼4−5 nm) with narrow size distributions. Bragg reflections revealed face-centered-cubic crystal symmetries for all the catalysts (Figure S3). Peak shifts toward higher diffraction angles with increasing initial Co content (Figure S3) indicate the lattice contraction induced by Co. The experimental lattice parameters match well with the theoretical values calculated based on Vegard's law using the initial atomic compositions (Figure S3), which suggests that the majority of the Co atoms are well alloyed with the Pt atoms.

Electrochemical Characterization. The mass activity, specific activity, and electrochemical surface area (ECSA) of the Pt_xCo/C and Pt/C catalysts are summarized in Table 2. The ECSAs of the catalysts were obtained from hydrogen-adsorption/desorption (HAD) analysis

by integrating hydrogen adsorption area from 0.08 to 0.4 V in the cyclic voltammograms (CVs) at 20 mV/s scan rate (Figure 1). Each of the Pt_xCo/C catalysts exhibit marked enhancement in SA and MA over pure Pt/C, and the highest activity enhancements (6.2 times and 4.5 times in MA and SA) are comparable to those of the dealloyed Pt_1Co_1/C and $PtCo_3/C$ NP catalysts,[33,38] as well as other M-rich dealloyed Pt_xM ($x < 1$) NPs (4−8 times higher in MA and SA),[26,31] albeit with low initial Co content. Although the activity in general increases with increasing initial Co content, a strictly monotonic activity−composition correlation is not observed as the Pt_2Co/C is not more active than the Pt_3Co/C. Thus, the activity trends cannot be fully accounted for by the monotonic lattice contraction trend of these catalysts as expected from compressive−strain effects.[17,18,31,32] To elucidate the origin of the increasing activity trends with Co content, as well as the cause of the breakdown, *in situ* XAS measurements were performed to identify the atomic structure of the catalysts under *in situ* operating conditions.

In Situ XAS Characterization

Δμ-XANES Analysis (Surface Structure). For all the catalysts, the Pt white line intensity increases with applied potentials (Figure 2), which is caused by the charge transfer from Pt to the oxygenated species (such as hydroxyl intermediate (*OH)) accumulated on the surface under high potentials.[7,8,23,46] The high Pt white line intensity of the *ex situ* electrodes indicates their surfaces are largely covered by oxygenated species. Unlike Pt, which can adsorb and desorb oxygenated species repeatedly during voltage cycling, the Co on the surface is spontaneously oxidized when exposed to air, and the soluble Co oxides are quickly dissolved during the conditioning pretreatment in acidic electrolyte, accounting for the drastic reduction of the Co white line intensity of Pt_2Co/C (Figure 2, top right) and Pt_3Co/C NPs. As for catalysts with low Co content (Pt_4Co/C, Pt_6Co/C, and Pt_7Co/C (Figure 2, bottom right)), the Co X-ray absorption near-edge spectroscopy (XANES) between the *ex situ* and *in situ* electrodes are similar, indicating the low population of the exposed Co on the near-surface region. More importantly, the Co XANES of all the Pt_xCo/C catalysts remain unchanged with varying potentials (Figure 2 right), which shows that the majority of Co atoms are located inside the NPs without being directly exposed to the electrochemical environment. Therefore, it is clear that all the Pt_xCo/C NPs have Pt−Co cores covered by a Pt surface ($Pt_{surf}@PtCo_{core}$) under *in situ* acidic environment. The drastic difference in XANES between the dry electrode and the electrode under *in situ* electrochemical control highlights the necessity of characterizing the electrode under *in situ* conditions.

$\Delta\mu$ analysis is conducted only on the Pt L_3 edge XANES, as the Co K edge XANES does not change significantly with applied potentials. The $\Delta\mu$, defined as $\Delta\mu = \mu(A/Pt) - \mu(Pt)$, is surface sensitive because it involves the difference between the XAS absorption when adsorbates are present, $\mu(A/Pt)$, and the signal from a nearly adsorbate-free Pt surface, $\mu(Pt)$, thus highlighting the small changes occurring on the surface caused by the adsorption. It provides information about the nature of the adsorbate, the adsorbate coverage, and specific adsorption sites on the Pt.[46−49] As shown in Figure 3, all the Pt_xCo/C and Pt/C catalysts exhibit a $\Delta\mu$ peak with characteristic features of a Pt surface, which can be well mimicked by the $\Delta\mu$ signal

TABLE 2. Summary of RDE Results[a]

catalyst	Co:Pt (atomic ratio)	ECSA ($m^2 \cdot g^{-1}$)	MA ($A \cdot mg_{Pt}^{-1}$)	SA ($mA \cdot cm_{Pt}^{-2}$)
Pt_2Co/C	0.48	47.6 ± 1.2	0.477 ± 0.022	1.00 ± 0.03
Pt_3Co/C	0.36	53.8 ± 0.8	0.539 ± 0.023	1.00 ± 0.03
Pt_4Co/C	0.25	52.7 ± 0.9	0.421 ± 0.038	0.80 ± 0.04
Pt_6Co/C	0.16	43.9 ± 2.4	0.275 ± 0.019	0.63 ± 0.03
Pt_7Co/C	0.14	49.0 ± 3.9	0.333 ± 0.031	0.68 ± 0.04
Pt/C	0	39.1 ± 3.6	0.087 ± 0.011	0.22 ± 0.02

[a] At least 3 RDE measurements were conducted for each catalyst. The ± indicates standard deviation.

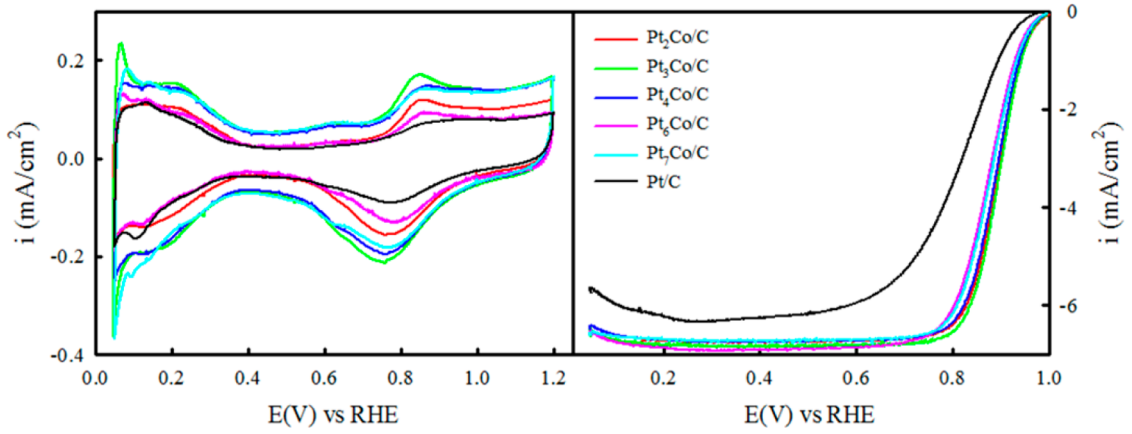

Figure 1. Cyclic voltammograms of the catalysts taken in N_2-purged 0.1 M $HClO_4$ at a scan rate of 20 $mV \cdot s^{-1}$ (left); ORR voltammograms of the catalysts taken in O_2-purged 0.1 M $HClO_4$ at a scan rate of 5 $mV \cdot s^{-1}$ (right).

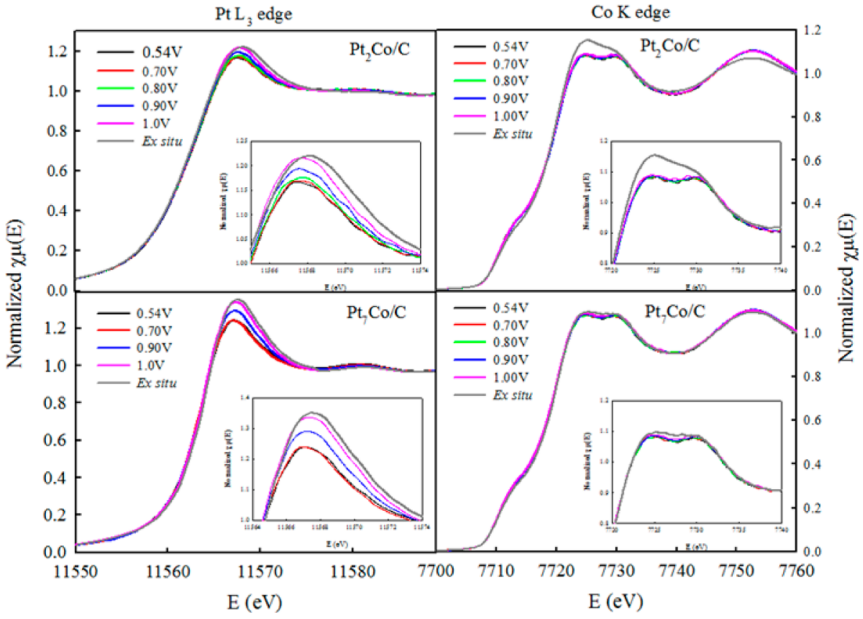

Figure 2. Pt L_3 edge (left) and Co K edge (right) XANES spectra of Pt_2Co/C and Pt_7Co/C in N_2-purged 0.1 M $HClO_4$ at various potentials.

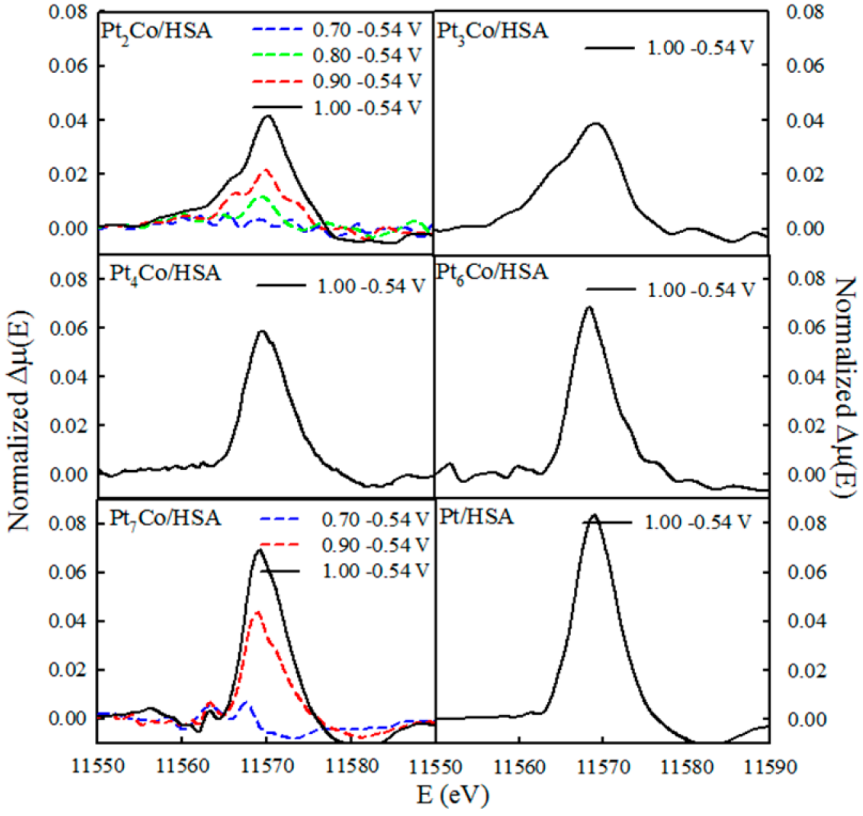

Figure 3. $\Delta\mu$ spectra of Pt_xCo/C and Pt/C catalysts obtained by subtracting the XANES at the Pt L_3 edge collected at 0.54 V from various potentials in N_2-pruged 0.1 M $HClO_4$ ($\Delta\mu = \mu(V) - \mu(0.54\ V)$). The $\Delta\mu$ spectra of Pt_2Co/C and Pt_7Co/C are derived from the Pt L_3 edge spectra in Figure 2.

given by the theoretical multiple scattering FEFF8[50] calculations using a Pt_6 or Pt_{25} cluster with or without adsorbates, as reported many times previously in the literature.[46−49,51,52] This further confirms the Pt-dominant surface of all the Pt_xCo/C catalysts. The monotonic increase in $\Delta\mu$ magnitude with increasing potential reflects the increase in adsorbate coverage with applied potentials. This adsorbate coverage measured in O_2-free solutions has been widely related to the ORR activities of Pt−alloy

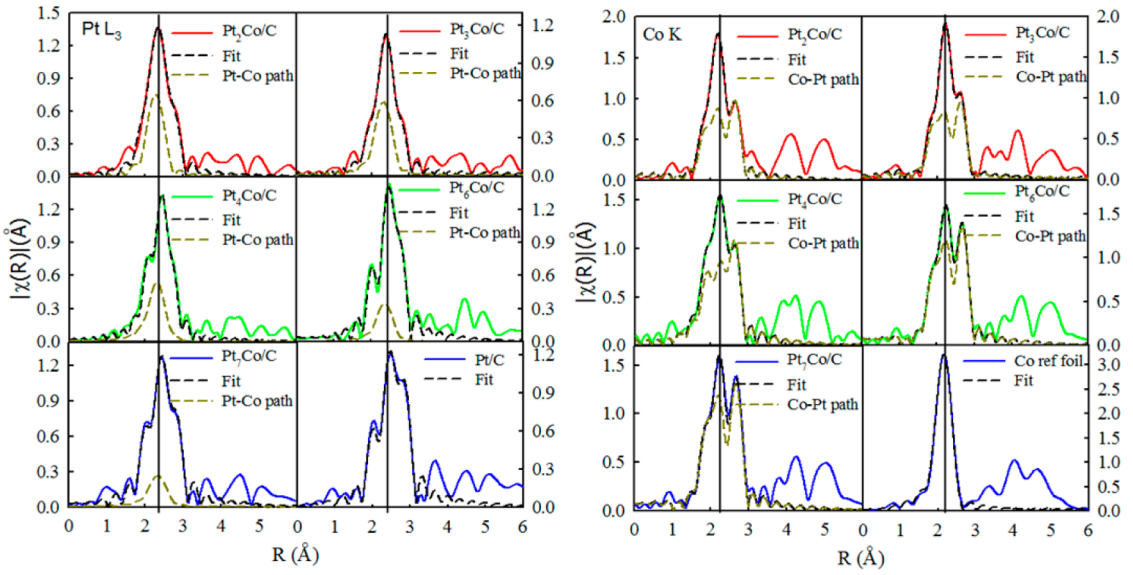

Figure 4. Pt L_3 edge (left) and Co K edge (right) EXAFS spectra collected at 0.54 V in N_2-saturated 0.1 M $HClO_4$ electrolyte and the corresponding least-squares fits for BOL and 5k-cycled (Figure S6) Pt_xCo/C and Pt/C NP catalysts. The fit of the Co reference foil data is also included for comparison. The vertical black lines are drawn as guides to the eye. As the Co/Pt atomic ratio decreases, the Pt−Co scattering peak intensity decreases and the Co−Pt scattering peak intensity increases, accompanied by a right shift of the main FT peaks.

TABLE 3. Summary of EXAFS Results[a]

		R_{Pt-Pt}	R_{Pt-Co}	R_{Co-Co}	N_{Pt-Pt}	N_{Pt-Co}	N_{Co-Co}	N_{Co-Pt}			
catalyst	cycling stage	($\Delta R = \pm 0.008$ Å)[b]			($\Delta N = \pm 0.9$)[b]		($\Delta N = \pm 0.5$)[b]		R_f	J_{Pt}	J_{Co}
Pt_2Co/C	0 k	2.703	2.645	2.636	5.5	2.7	3.7	8.5	0.010	1.36	0.92
	5 k	2.719	2.647	2.610	6.8	1.9	4.9	7.1	0.011	1.03	0.75
Pt_3Co/C	0 k	2.699	2.663	2.643	5.7	2.5	3.5	8.4	0.008	1.33	0.91
	5 k	2.721	2.662	2.606	7.1	1.7	4.2	7.7	0.011	1.07	0.79
Pt_4Co/C	0 k	2.713	2.662	2.640	6.3	2.2	3.6	8.5	0.010	1.26	0.88
	5 k	2.723	2.659	2.631	6.6	1.9	3.8	8.3	0.010	1.2	0.84
Pt_6Co/C	0 k	2.730	2.699	2.654	9.0	1.7	0.8	11.6	0.013	1.24	1.07
	5 k	2.739	2.696	2.655	9.0	1.4	1.6	11.4	0.017	1.23	0.98
Pt_7Co/C	0 k	2.734	2.695	2.663	8.7	1.5	0.9	11.2	0.013	1.25	1.05
	5 k	2.743	2.696	2.672	9.1	1.2	1.2	11.5	0.007	1.23	1.00
Pt/C	0 k	2.756			9.9				0.006		
	5 k	2.757			10.4				0.006		

[a] S_0^2 fixed at 0.756 and 0.7 for Pt and Co, respectively, as obtained by fitting the reference foils. Fits were done in *R*-space, $k^{1,2,3}$ weighting. For Pt, $1.0 < R < 3.0$ Å and $\Delta k = 2.87 - 12.29$ $Å^{-1}$ were used; for Co, $1.0 < R < 3.0$ Å and $\Delta k = 1.80 - 11.75$ $Å^{-1}$ were used. R_f is a measure of the goodness of fit. [b] Values represent the largest statistical errors of all of the least-squares fits determined by ARTEMIS.

catalysts, as the adsorbates are believed to act as "poisons" to the active sites.[20,51,53]

EXAFS Analysis (Bulk Structure). Comprehensive Fourier transform (FT) EXAFS analysis, which involves analyzing the Pt L_3 edge, involving Pt−Pt and Pt−Co scattering, and the Co K edge, involving Co−Co and Co−Pt scattering, was conducted on beginning-of-life (BOL) and 5k-cycled Pt_xCo/C and Pt/C catalysts to explore their bulk structures at the atomic scale. For Pt_xCo/C catalysts, first-shell coordination number fitting is applied to both the Pt and Co edges concurrently. EXAFS data collected at 0.54 V (double-layer region where no evidence of electrochemical adsorbates such as H_{upd}, O_{ads}, and OH_{ads} was found on these Pt-based catalysts) and the first-shell fits for the Pt L_3 edge and Co K edge of the samples are shown in Figure 4 (the corresponding data in k space are provided in Figures S4 and S5). The fitting results are listed in Table 3. Basic constraints as follows are introduced for the fitting:

$$R_{Pt-Co} = R_{Co-Pt} \quad (1)$$

$$\sigma^2_{Pt-Co} = \sigma^2_{Co-Pt} \quad (2)$$

Here $R_{Pt-Co} = R_{Co-Pt}$ is the bond distance for Pt−Co (or Co−Pt) scattering; σ^2_{Pt-Co} and σ^2_{Co-Pt} are uncertainties in the bond lengths as suggested by the fitting.

The basic EXAFS analysis provides qualitative information on the cluster bulk morphology. The total

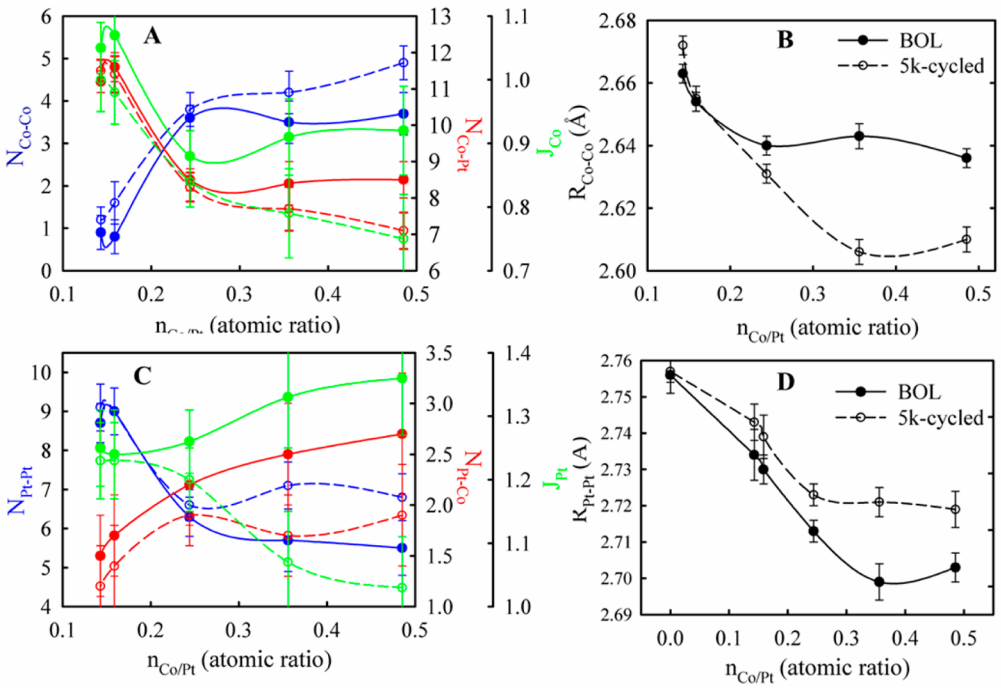

Figure 5. Coordination numbers and *J* values of the Co (A) and Pt (C) absorbers, and the Co−Co (B) and Pt−Pt (D) bond distances in the fresh (solid line) and 5k-cycled (dashed line) Pt_xCo/C and/or Pt/C catalysts as a function of the nominal Co/Pt atomic ratio.

coordination number of Co ($N_{Co} = N_{Co-Pt} + N_{Co-Co}$) for all the BOL catalysts is ~12, close to that in bulk Pt−Co alloys. This indicates the majority of the Co is fully coordinated and thus located in the inner part of the NPs. On the contrary, the total coordination number of Pt ($N_{Pt} = N_{Pt-Pt} + N_{Pt-Co}$) is smaller than that of Co because the Pt atoms on the surface are undercoordinated. These results further confirm the $Pt_{surface}$@ $PtCo_{core}$ structure of all the Pt_xCo/C catalysts, as suggested by $\Delta\mu$-XANES analysis.

As for core−shell PtM NPs, the EXAFS data at the Pt and M edges are averaged throughout the entire cluster ($Pt_{shell} + PtM_{core}$) and the whole PtM core, respectively, owing to the bulk nature of XAS. The bulk atomic distribution of Pt and M can thus be quantitatively evaluated by the *J* values derived from the coordination numbers (a detailed explanation of the *J* value is given in the Supporting Information).[54] However, the atomic concentration gradient within the core, if there is any, cannot be explored by the typical EXAFS analysis or other techniques under operating conditions. To address this problem, all the catalysts were subjected to a modest voltage cycling (5000 cycles) to preferentially remove the Co from the near-surface region.[29,30] The EXAFS data of the cycled samples reveal the morphology of the PtCo inner core under *in situ* conditions and thereby provide unique insight into the concentration gradient within the PtCo core when combined with the EXFAS data of the BOL samples.

The main output of the EXAFS analysis is summarized in Figure 5, where the coordination numbers, the *J* values, and the bond distances of the BOL (solid lines) and 5k-cycled (dashed) Pt_xCo/C and Pt/C catalysts are plotted as a function of the initial Co/Pt ratio. The PtCo core morphology is probed by analyzing the EXAFS data at the Co K edge (Figure 5A and B). When $n_{Co/Pt}$ is ~0.15 (Pt_6Co/C and Pt_7Co/C), the Co atoms are surrounded by mostly Pt atoms ($N_{Co-Co} \approx 1$ and $N_{Co-Pt} \approx 11$) and statistically distributed in the cores without Co segregation ($J_{Co} \approx 1$). When $n_{Co/Pt}$ is increased to ~0.25, N_{Co-Co} sharply increases to 3.6 while N_{Co-Pt} drastically decreases to 8.5, with consequent drop of J_{Co}. This indicates the formation of concentrated Co in the cores with increasing Co content. Interestingly, further increase of $n_{Co/Pt}$ does not change the values of N_{Co-Co}, N_{Co-Pt}, and J_{Co} significantly, and these values are close to those of a perfectly disordered Pt_3Co model (N_{Co-Co} = 3, N_{Co-Pt} = 9, J_{Co} = 1). This appears to suggest the formation of a disordered Pt_3Co core for these catalysts. However, the J_{Co} and N_{Co-Pt} of the Pt_2Co/C and Pt_3Co/C catalysts drop significantly upon 5k cycles, which indicates that the Co atoms in the inner cores (survived the cycling) are surrounded by less Pt neighbors than the Co atoms in the near-surface region (removed by cycling). This is further confirmed by the drastic reduction in R_{Co-Co} upon cycling for these two catalysts (Figure 5B), as the R_{Co-Co} in the Co-rich cores is expected to be shorter than that in the Pt-rich near-surface region according to Vegard's law. Also we noticed the J_{Co}, N_{Co-Pt}, and R_{Co-Co} of the cycled samples generally decrease with increasing $n_{Co/Pt}$, which clearly shows that the Co concentration in the inner cores generally increases with increasing

$n_{Co/Pt}$. Thus, we conclude that the Pt_2Co/C and Pt_3Co/C catalysts possess a Co concentration gradient such that some Co is concentrated in the inner cores and gradually depletes within the Pt-rich near-surface region. On the contrary, the J_{Co}, N_{Co-Pt}, and R_{Co-Co} of the Pt_xCo/C catalysts with low Co content ($x \geq 4$) do not change significantly with voltage cycling, as these catalysts do not possess Co-populated near-surface regions and Co-concentrated inner cores, and thus exhibit a relatively uniform distribution of Co rather than a Co concentration gradient.

The similar analysis on the Pt L_3 edge further supports the conclusions regarding the atomic distribution drawn from the Co K edge data and also provides additional information regarding the Co loss during cycling. The local coordinate environment of Pt exhibits an expected trend with increasing $n_{Co/Pt}$ ratio: the N_{Pt-Co} increases and the N_{Pt-Pt} decreases, with consequent drop of J_{Pt} (Figure 5C). In addition, the R_{Pt-Pt} generally decreases with increasing $n_{Co/Pt}$ as expected from Vegard's law, except that the R_{Pt-Pt} between Pt_2Co/C and Pt_3Co/C NPs is comparable. Note this R_{Pt-Pt} trend differs from the monotonic lattice parameter trend as revealed by *ex situ* XRD (Figure S3b). The increase in the R_{Pt-Pt} for all the Pt_xCo/C NPs after 5000 cycles (Figure 5D) is ascribed to the Co loss upon cycling, and the bigger R_{Pt-Pt} relaxation observed for Pt_2Co/C and Pt_3Co/C points to the higher Co loss. This is further supported by the drastic drop of the N_{Pt-Co} observed for these two catalysts. The corresponding drop of the J_{Pt} indicates that the Co atoms well alloyed with Pt are preferentially removed, which further confirms it is indeed the Co atoms in the near-surface region that are leached out as seen from the Co side. The less Co loss upon the cycling for Pt_xCo/C NPs with low Co content ($x \geq 4$) is due to the low Co population in the near-surface region.

Scheme 1 illustrates our findings of the *in situ* atomic structure of the Pt_xCo/C NPs with varying Co/Pt ratio obtained from $\Delta\mu$-XANES and EXAFS analysis. All the Pt_xCo/C NPs possess the $Pt_{surface}@PtCo_{core}$ structure under operating conditions. The Pt_xCo/C NPs with high Co content (Pt_2Co/C and Pt_3Co/C) possess a Co concentration gradient such that some Co is concentrated in the cores and gradually depletes within the Pt-rich near-surface region; contrarily the Pt_xCo/C NPs with low Co content (Pt_4Co/C, Pt_6Co/C, and Pt_7Co/C) possess a relatively uniform distribution of Co with low Co population in the near-surface region. The Pt_xCo/C NPs with high Co content are subjected to big Co loss during the acid pretreatment and the voltage cycling because the Co in the near-surface region is susceptible to acid dissolution.

DISCUSSION

Structure–Activity Correlation: Compressive-Strain Effects. As for core–shell PtM NPs, the surface compressive strain originating from the lattice mismatch between the Pt-rich surface and the M-rich core is believed to play a dominant role in improving their ORR activity *via* altering the electronic properties (such as d-band center) of surface Pt.[31] Unfortunately, quantification of the surface compressive strain requires measuring surface R_{Pt-Pt} under working conditions, and this has proven to be very challenging if not impossible. Attempts to derive the surface R_{Pt-Pt} from the bulk R_{Pt-Pt} for real operating PtM NP catalysts are deemed to be fruitless (a detailed discussion is given in the Supporting Information). It is thus tempting to examine whether the bulk average R_{Pt-Pt}, which can be readily measured under operating conditions by XAS, can serve as a valid descriptor for compressive-strain effects. Accordingly, the compressive strain is defined here as

$$S = \frac{R^{PtCo}_{Pt-Pt} - R^{Pt}_{Pt-Pt}}{R^{Pt}_{Pt-Pt}} \times 100\% \quad (3)$$

where R^{PtCo}_{Pt-Pt} and R^{Pt}_{Pt-Pt} are the bulk average Pt–Pt bond distances in the Pt_xCo/C and Pt/C samples obtained by EXAFS, respectively (Table 3). Note the compressive strain is overestimated here, as the bulk R_{Pt-Pt} determined by EXAFS is expected to be shorter than the surface R_{Pt-Pt} owing to the surface relaxation.[31,55]

As shown in Figure 6 left, the intrinsic SAs of the Pt_xCo/C and Pt/C increase nearly linearly with decreasing R_{Pt-Pt} or increasing strain. As these catalysts possess a narrow range of ECSA (Table 2), a linear correlation between their MA and R_{Pt-Pt} is also observed. These results demonstrate that the compressive strain plays a dominant role in determining the ORR activity of the Pt_xCo/C NP catalysts and can

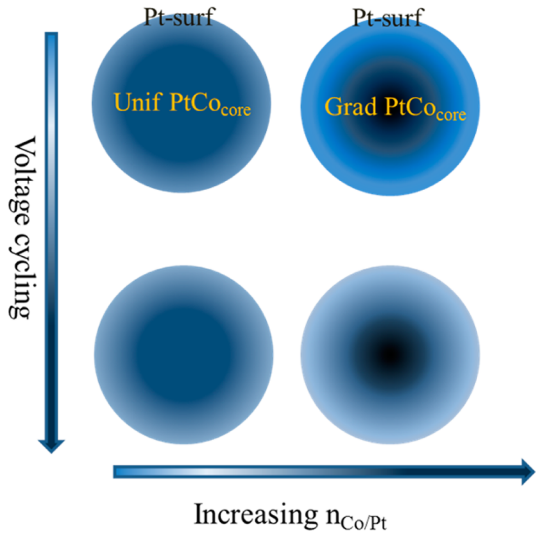

Scheme 1. Representation of the atomic distribution of the core–shell Pt_xCo/C NPs under *in situ* conditions changes with initial Co/Pt atomic ratio and voltage cycling. The darker color represents the higher Co concentration.

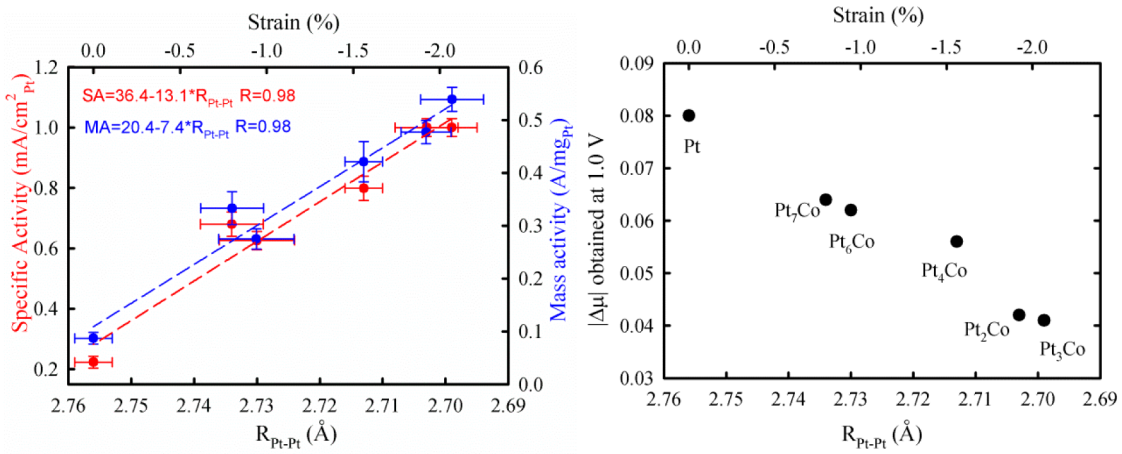

Figure 6. Measured specific (red) and mass (blue) activities (left) and the $\Delta\mu$ amplitude derived from Figure 3 ($|\Delta\mu| = |\mu(1.0\ V) - \mu(0.54\ V)|$) (right) of the Pt_xCo/C and Pt/C as a function of R_{Pt-Pt} or the strain (upper *x*-axis). The dashed lines are the linear fitting results, and the corresponding equations and *R* values are given in the figure.

be represented by the bulk R_{Pt-Pt}. This implies that the bulk and surface R_{Pt-Pt} are strongly correlated despite the surface relaxation. This is likely because the surface strain induced by the core−shell lattice mismatch only gets gradually released for more than 5 Pt layers[19] and, thus, remains largely intact for small NPs with limited atomic layers. In addition, for Pt_xCo/C NPs with low Co content, the surface relaxation is mild due to the relatively weak surface strain. For Pt_xCo/C NPs with high Co content, the strong surface relaxation tendency to relieve some of the intensive strain is however suppressed by the populated Co in the near-surface region.[41] Thus, we conjecture that the Pt_xCo/C NPs with different Co content are subjected to a comparable level of surface relaxation, which may also account for the strong correlations between the bulk and the surface R_{Pt-Pt}. Nevertheless, the linear correlation between the bulk R_{Pt-Pt} and the ORR activity of Pt_xCo/C NPs found in this work shows that the bulk R_{Pt-Pt} is a valid strain descriptor as the alternative to the surface R_{Pt-Pt}, which makes it possible to correlate the catalytic performance of PtM NP catalysts to a property that can be measured under ORR operating conditions.

To gain in-depth insights into the fundamental role played by compressive strain, we show in Figure 6, right, $\Delta\mu$ magnitudes ($|\Delta\mu|$), which derive from the maximum magnitude of the $\Delta\mu$ signals displayed in Figure 3, as a function of the bulk R_{Pt-Pt} or the strain. The $|\Delta\mu|$ obtained in the absence of O_2 originates exclusively from water activation. It reflects the changes in poisonous *OH coverage and Pt−O bond strength of PtM NPs and tracks well with their ORR activity.[18,47,49,51] Figure 6 right shows that the $|\Delta\mu|$ generally decreases with increasing compressive strain. This, together with the Pt d-band center downshifting with decreasing R_{Pt-Pt} as obtained by FEFF (Figure S7)[18] or density functional theory (DFT)[17] calculations, confirms that compressive strain weakens the Pt−O bond strength by downshifting the Pt d-band center and thereby enhances the ORR rate by suppressing the *OH adsorption that blocks surface sites from the O_2 reactant.

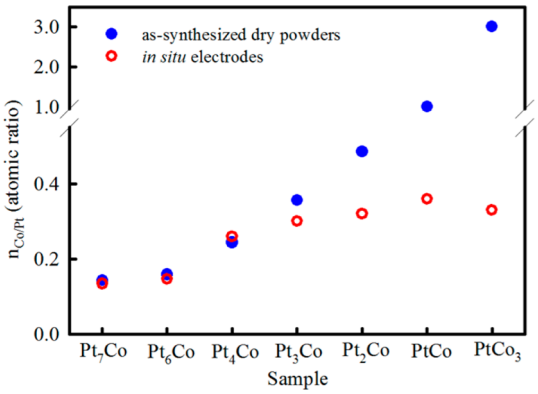

Figure 7. Co/Pt atomic ratio of the Pt_xCo/C catalysts obtained by *ex situ* element analysis (dots) and obtained using the experimentally determined coordination numbers (Table 3) (circles). The data of PtCo/C and $PtCo_3$/C catalysts in refs 33 and 38 are included for comparison purposes.

Composition−Strain Correlation: Vegard's Law. As the bulk R_{Pt-Pt} of the Pt_xCo/C NPs is linearly related to the ORR activity, it is of particular interest to identify what controls the bulk R_{Pt-Pt}. A monotonic correlation between the bulk R_{Pt-Pt} and the nominal atomic composition is not observed (Figure S8). This is likely caused by the different Co loss extent during the acid pretreatment for the Pt_xCo/C catalysts with different initial Co content as suggested by $\Delta\mu$-XANES and/or the different atomic distribution revealed by EXAFS. To test the hypothesis, we present in Figure 7 the Co/Pt ratios of the as-synthesized Pt_xCo/C dry powders and the corresponding *in situ* electrodes under electrochemical control, in addition to the results of the dealloyed PtCo/C and $PtCo_3$/C NPs reported by us previously.[33,38] The *in situ* Co/Pt atomic ratio is derived from the

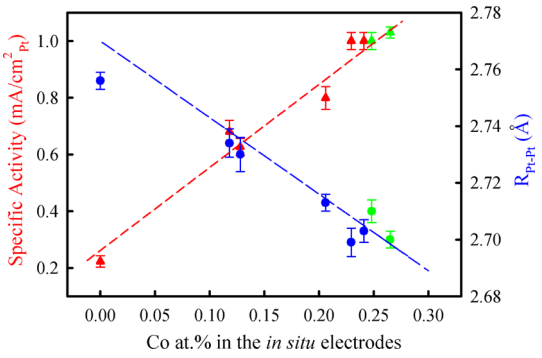

Figure 8. Specific activity (red triangle) and R_{Pt-Pt} (blue dots) of Pt_xCo/C and Pt/C NPs are displayed as a function of the Co content determined by EXAFS. The specific activity (green triangle) and R_{Pt-Pt} (green dots) of dealloyed PtCo/C and $PtCo_3$/C catalysts reported in refs 33 and 38 are also included. The R_{Pt-Pt} calculated using the *in situ* Co/Pt atomic ratio based on Vegard's law is shown (blue dashed line) for comparison. The slight deviations observed for Pt/C are caused by the shorter R_{Pt-Pt} of small Pt NPs (~2.75 Å) compared to that of bulk Pt (2.77 Å)[59] used for Vegard's law calculations. The red dashed line is a guide to the eye.

experimentally measured coordination numbers (Table 3) following the equation[56]

$$n_{Co/Pt} = \frac{N_{Pt-Co}}{N_{Co-Pt}} \quad (4)$$

Figure 7 clearly shows that the Pt_xCo/C NPs with initially higher Co content are subjected to bigger Co loss during the acid pretreatment. This is because (i) the Pt_xCo/C NPs with initially high Co content contain some Co in the near-surface region that is prone to acid dissolution, as evidenced by $\Delta\mu$-XANES and EXAFS analysis, and (ii) the Co dissolution can retreat from the surface region toward the inner core of the Pt_xCo/C NPs with high enough Co content that the leaching rate of Co exceeds the surface diffusion of Pt.[29,30,57] As a result, the residual Co contents in dealloyed PtCo/C and $PtCo_3$ are comparable to those of Pt_3Co/C and Pt_2Co/C despite their higher initial Co content. Correspondingly, the R_{Pt-Pt}(s) in these NPs are very close (Figure 8). This unambiguously confirms that the R_{Pt-Pt} of Pt_xCo/C NPs is related to the residual rather than initial Co content. Indeed, Figure 8 shows that for all the Pt–Co/C NPs the experimental R_{Pt-Pt} values match well with those calculated using the residual Co content based on Vegard's law, despite their dissimilar atomic structures. This also suggests that the bulk R_{Pt-Pt} of PtM NPs, or the compressive strain, is predominantly determined by the atomic composition and insensitive to the atomic distribution. The particle size effects on R_{Pt-Pt} wear out for Pt/C NPs bigger than 3 nm[58,59] and are thus negligible here given that the majority of the Pt_xCo/C NPs are greater than 3 nm (Table 1 and Figure S2).

As the SA was shown to be linearly related to the bulk R_{Pt-Pt} (Figure 6), a nearly linear correlation between the SA and the *in situ* Co/Pt ratio is expected (Figure 8). The linear correlations established between the ORR activity and the bulk R_{Pt-Pt} and between the bulk R_{Pt-Pt} and the *in situ* atomic composition demonstrate that the bulk R_{Pt-Pt} is a valid descriptor for compressive-strain effects and nicely bridges the atomic composition and the ORR activity of PtM NP catalysts. On the contrary, a linear composition–strain–activity was not observed when adopting the initial Co/Pt atomic ratio (Figure S8). The linear composition–strain–activity correlation of the Pt_xCo/C NP catalysts clearly shows that their enhanced ORR activity over pure Pt originates primarily from the strain induced by Co and is controllable by tuning the *in situ* atomic composition.

Although the linear composition–strain–activity correlation is demonstrated on the Pt–Co system here, it is not necessarily limited to this system since the key factor, strain, is governed by the universal Vegard's law. To test this hypothesis, a similar XAS analysis procedure was repeated on a series of dealloyed Pt_xNi/C NP catalysts that were recently demonstrated to exhibit record ORR activity and durability in PEMFCs.[35–37] Again, the R_{Pt-Pt} is linearly related to the Ni/Pt atomic ratio of the electrode in a PEMFC as governed by Vegard's law (Figure S9a). The specific activities of the catalysts exhibit a volcano curve as a function of R_{Pt-Pt} as expected from Sabatier's principle of catalysis (Figure S9a), but a linear correlation between the R_{Pt-Pt} and SA is clearly seen on the weak Pt–O binding leg of the volcano (the region studied in this work), accompanied by a monotonic trend of $|\Delta\mu|$ (Figure S9b). Interestingly, this linear SA–strain correlation on the weak binding leg of the volcano curve was predicted by DFT calculations on a Pt(111) single-crystal slab under isotropic strain (Figure 6 in ref 31). In the same figure the nearly linear correlations between the ORR activity of dealloyed $PtCu_x$/C catalysts and the strain are also presented.[31] In addition to the Pt–M systems where M represents the late 3d elements, most recently Chorkendorff *et al.*[60] observed a monotonic relation between the activity of Pt_xY and the surface R_{Pt-Pt} derived from *ex situ* EXAFS fits and thereby attributed the enhanced ORR activity over pure Pt exclusively to the strain. These results clearly show that the ORR activity descriptor, R_{Pt-Pt}, identified in this study is applicable to a wide variety of Pt-based catalyst systems.

The ORR activity of Pt-based catalysts is, broadly speaking, impacted by the interplay of strain, ligand, and particle size effects. The ligand effects in the studied Pt_xCo/C NPs are negligible (if there are any) compared to the concurrent compressive-strain effects, as expected from the theoretical calculations on the Pt–Co system.[16,18] Given that the SA of Pt/C increases linearly as particle size grows from ~2 nm to 10 nm, accompanied by a drastic drop of the ECSA,[61] the particle size effects to a large extent are

deconvoluted here since the Pt_xCo/C NPs possess comparable mean particle sizes (~4−5 nm) with narrow size distributions (Table 1), which is further supported by the narrow range of their ECSAs (Table 2). As for catalysts in which the ligand and/or particle size effects play important roles in affecting their ORR activities, the linear composition−strain−activity correlation does not hold. For instance, Antolini *et al.*[62] reported that the ORR activity of Pt−Co/C catalysts was poorly related to the bulk R_{Pt-Pt} owing to the wildly different particle sizes of these catalysts, but presented a linear relationship with the integrated intensity of the Pt L_3 edge at 1.1 V because this parameter takes into account both strain and particle size effects. However, ligand effects[17] are induced by the less noble M atoms in the immediate subsurface that are prone to acid dissolution and thus are devoid or vanish rapidly in PtM catalysts in the highly corrosive and oxidizing conditions at a PEMFC cathode. Particle size effects are essentially related to the abundance of the {111} sites, which increases with increasing particle size.[61] Despite recent progress in developing Pt-based NP catalysts with enriched {111} facets,[11,63,64] translation of these conceptual systems to practical PtM NP catalysts that sustain long-term PEMFC operation has been largely unsuccessful since small NPs tend to exist as truncated octahedrons to minimize free energy.[65] The most active and durable ORR catalysts tested in PEMFCs so far are the dealloyed PtM catalysts,[26,36] for which the enhanced ORR activities are predominantly attributed to the strain effects.[31,37] In this regard, the strain descriptor R_{Pt-Pt} links directly to the ORR activity of practical PtM catalysts in an operating PEMFC.

The linear composition−strain−activity correlation has important implications on the development of active and durable PtM cathode catalysts. The ORR activity of PtM catalysts is limited by the M leaching during the acid pretreatment (Figure 7). Likewise, the durability of PtM catalysts is essentially limited by the M leaching during PEMFC operation. Therefore, suppressing M leaching in acidic environments is expected to increase the ORR activity and durability of PtM catalysts. One facile pathway to suppress the M leaching is to reduce the nanoporosity of the PtM NPs.[66] This work suggests M leaching suppression can also be achieved by increasing the Pt overlayer thickness, as the M atoms in the near-surface region are prone to acid dissolution as compared to those buried in the core. This is not necessarily compensated by the attenuation of the compressive strain, which has a long effective range and is insensitive to the atomic distribution. These implications are confirmed by our recent development of dealloyed $PtNi_3/C$ catalysts with nonporous and ultrathick (~1.2 nm) Pt overlayers.[35−37] These catalysts exhibit record ORR activity and durability in PEMFCs, which was attributed to their extraordinary Ni retention against the dealloying process (thus high Ni content in BOL catalysts) and the extensive voltage cycling in PEMFCs (thus high Ni content in aged catalysts).

CONCLUSIONS

In summary, this work has shown that the ORR activity of the Pt_xCo/C and Pt/C NPs is linearly related to their bulk average Pt−Pt bond length (R_{Pt-Pt}) determined under *in situ* operating conditions, and the R_{Pt-Pt} contracts linearly with an increase in *in situ* Co/Pt atomic ratio, as expected from Vegard's law. This linear composition−strain−activity correlation conclusively shows that the ORR activity enhancement of the Pt_xCo/C NPs over pure Pt/C originates from the strain induced by Co substitution in the Pt lattice, and the strain is controllable by tuning the atomic composition. These findings highlight that the R_{Pt-Pt} can serve as a valid descriptor for compressive-strain effects and nicely bridges the atomic composition and the ORR activity of Pt-based catalysts. The atomic distribution of Co in the Pt_xCo/C NPs is shown to be strongly dependent on the Co/Pt atomic ratio: the Pt_xCo/C NPs with high Co content ($x \leq 3$) possess a Co concentration gradient such that some Co is concentrated in the core and gradually depletes within the Pt-rich surface region, whereas the Pt_xCo/C NPs with low Co content ($x \geq 4$) possess a relatively uniform distribution of Co with low Co population in the near-surface region. The atomic distribution does not affect the ORR activity significantly, whereas it may play an important role in affecting the durability, as the Co atoms located in the near-surface region are prone to acid dissolution, and the corresponding activity gains are not sustained in long-term operations. This composition−strain−activity correlation provides guidance in selecting the synthesis procedures for tuning Pt shell thicknesses, core structures, and overall particle compositions necessary for rational optimization of the ORR activity of Pt-based catalysts.

EXPERIMENTAL SECTION

RDE Testing. Pt_xCo/C ($x = 2$ to 7) and Pt/C catalysts were made by Tanaka Kikinzoku Kogyo (TKK) Inc. for Automotive Fuel Cell Cooperation Corporation (AFCC). The required amount of catalyst was weighed in a static-eliminated 40 mL glass vial followed by 25 g of 18 MΩ deionized water, 5 g of 2-propanol (ACS grade, Alfa Aesar), and perfluorosulfonic acid−PTFE copolymer (5.3% w/w solution, Alfa Aesar). Deionized water was added to wet the dry catalyst powder to prevent the catalyst from burning prior to the addition of 2-propanol and copolymer. The amount of dry copolymer in the electrode is about 12 wt %. A horn sonicator (Sonifer, model S-450D, disruptor horn, Branson) was used to disperse the catalyst in the solvent mixture at 65% amplitude with 1/1 s ON/OFF pulse

intervals for an accumulated 15 min ON time or 30 min total time. During sonication the sample vial was immersed in an ice bath to keep the solvents from evaporating.

Immediately after sonication, 10 μL of ink was pipetted on the glassy carbon disk mounted on a rotator. Then the disk was covered with a glass beaker to prevent dust contamination and rotated at 700 rpm starting within seconds. A table lamp was used to accelerate the drying process. Ink was allowed to dry at 700 rpm for about 25 min. Caution was exercised not to overdry the catalyst, as this may result in flaking of the electrode. The target catalyst loading on the glassy carbon disk is about 10 $\mu g_{Pt}/cm^2$. The electrochemical cell was filled with 0.1 M perchloric acid (diluted from 70% double-distilled acid, GFS Chemicals), and the Pt counter electrode and partially H_2 filled Pt reference electrode were inserted into the cell. The temperature of the cell was maintained at 30 °C by circulating water using a thermostat. All voltages reported were with respect to RHE. The rotating disk electrode was cleaned by cycling the potential between 0.05 and 1.2 V for 100 cycles at a scan rate of 1 V/s in N_2. ECSA for the catalysts was calculated by integrating the hydrogen desorption area of the voltammogram taken at 20 mV/s scan rate. The columbic charge for a monolayer hydrogen desorption on smooth Pt is assumed to be 0.21 mC/cm^2. Oxygen was bubbled during ORR measurements, and the electrode was cycled between 1.00 and 0.05 V. The reverse scan (anodic) from 0.05 V to 1.00 V was used to determine the mass and specific activities of the catalyst at 0.9 V.

Microscopic Experiments. Particle morphology, compositional measurements, and elemental analysis were performed with a Hitachi S-4800 field emission scanning electron microscope, combined with its EDS module, and a JEOL 2010 field emission gun transmission electron microscope.

X-ray Diffraction Experiments. Analysis was conducted *via* a Bragg−Brentano para-focusing UltimaIV powder diffractometer utilizing a Cu Kα radiation source from Rigaku. Unit cell constants of the samples were refined with the PDXL software program provided by Rigaku Corporation.

XAS Experiments. The electrode inks for the XAS electrodes were composed of 8.2 MΩ purity deionized water (Millipore), 2-propanol (HPLC-grade, Aldrich), 5 wt % Nafion solution (Aldrich), and the catalyst powder. The composition was chosen to give a final electrode with a dry Nafion loading of 5 wt %. The ink was hand-painted onto a Zoltek carbon cloth and dried for 15 min in a 65 °C vacuum oven between coats. The final Pt and Co geometric loadings were chosen to give 0.05 transmission spectra edge heights at the Pt L_3 and Co K edges, respectively. The aged samples were obtained by cycling the beginning-of-life (after around 100 cycles) electrodes between 0.1 and 1.0 V in a square wave cycle with 2 s hold at each potential for 5000 cycles in a previously described *in situ* spectro-electrochemical half-cell.[67] Note that the voltage cycling conducted in the spectro-electrochemical half-cell here is to explore the atomic distribution of the samples by preferentially dissolving the soluble metal (Co here), rather than evaluate the durability that is typically conducted in a RDE or a PEMFC. The XAS experiments were conducted on both BOL and aged samples at room temperature in the same half-cell through which continuously sparged (N_2 or O_2) 0.1 M $HClO_4$ was circulated. The samples are conditioned in 0.1 M $HClO_4$ under vacuum for 45 min to remove surface oxides and contaminants before being transferred into the half-cell. Potentiostatic control was maintained with an Autolab PGSTAT30 potentiostat/galvanostat (Metrohm USA, formerly Brinkman Instruments). The voltage cycling limits were 0.05 to 1.1 V. The electrode was fully cycled following each potential hold in order to clean the catalyst surface after each potential hold. Before each measurement, the cell was held for 5 min to reach a pseudo-steady state. Data collection was then performed at the chosen potentials held during anodic sweeps. All data were collected in the fluorescence mode at the beamlines of X3B and X19A at the National Synchrotron Light Source (NSLS) (Brookhaven National Laboratory, NY, USA). All of the experimental data were collected in conjunction with the appropriate reference foils to aid in energy alignment and normalization.

The data were processed and fitted using the Ifeffit-based Athena[68] and Artemis[69] programs. Scans were calibrated, aligned, and normalized with background removed using the IFEFFIT suite.[70] The $\chi(R)$ were modeled using single scattering paths calculated by FEFF6.[50]

The $\Delta\mu$-XANES analysis technique has been described in great detail elsewhere.[46−48,71] Briefly, difference spectra were calculated using the equation

$$\Delta\mu = \mu(\mathrm{V}) - \mu(0.54\ \mathrm{V}) \quad (5)$$

where μ(V) is the absorption coefficient of the sample at a potential of interest and μ(0.54 V) is the reference signal at 0.54 V, which is considered the clean double-layer region for platinum, *i.e.*, free of any adsorbed H, O(H), or oxygen adsorbates.

Conflict of Interest: The authors declare no competing financial interest.

Supporting Information Available: Additional information including the SEM and TEM images, the XRD results, the original XAS spectra at the Pt L_3 and Co K edges in k space, the EXAFS fitting results of the 5k-cycled samples, and the specific activity as well as the R_{Pt-Pt} as a function of initial Co/Pt composition, and the R_{Pt-Pt}, specific activity, and $\Delta\mu$ magnitude of dealloyed Pt_xNi/C catalysts as a function of Ni/Pt ratio are provided in a supplementary file. This material is available free of charge *via* the Internet at http://pubs.acs.org.

Acknowledgment. This research was supported by Automotive Fuel Cell Cooperation Corporation. Use of the National Synchrotron Light Source (beamline X3B), Brookhaven National Laboratory, was supported by the U.S. Department of Energy, Office of Science, Office of Basic Energy Sciences, under Contract No. DE-AC02-98CH10886. This publication was made possible by the Center for Synchrotron Biosciences grant P30-EB-009998, from the National Institute of Biomedical Imaging and Bioengineering (NBIB). Support from beamline personnel Dr. Erik Farquhar and Mark Chance (X3B) are gratefully acknowledged. The dealloyed Pt_xNi/C catalyst precursors were provided by R. O'Malley and A. Martinez (Johnson Matthey). A. Kongkanand and T. E. Moylan (GM) performed the dealloying and MEA tests.

REFERENCES AND NOTES

1. Gasteiger, H. A.; Kocha, S. S.; Sompalli, B.; Wagner, F. T. Activity Benchmarks and Requirements for Pt, Pt-Alloy, and Non-Pt Oxygen Reduction Catalysts for PEMFCs. *Appl. Catal., B* **2005**, *56*, 9–35.
2. Wagner, F. T.; Lakshmanan, B.; Mathias, M. F. Electrochemistry and the Future of the Automobile. *J. Phys. Chem. Lett.* **2010**, *1*, 2204–2219.
3. Wang, Y.; Chen, K. S.; Mishler, J.; Cho, S. C.; Adroher, X. C. A Review of Polymer Electrolyte Membrane Fuel Cells: Technology, Applications, and Needs on Fundamental Research. *Appl. Energy* **2011**, *88*, 981–1007.
4. Stephens, I. E. L.; Bondarenko, A. S.; Gronbjerg, U.; Rossmeisl, J.; Chorkendorff, I. Understanding the Electrocatalysis of Oxygen Reduction on Platinum and Its Alloys. *Energy Environ. Sci.* **2012**, *5*, 6744–6762.
5. Debe, M. K. Electrocatalyst Approaches and Challenges for Automotive Fuel Cells. *Nature* **2012**, *486*, 43–51.
6. Bing, Y.; Liu, H.; Zhang, L.; Ghosh, D.; Zhang, J. Nanostructured Pt-Alloy Electrocatalysts for PEM Fuel Cell Oxygen Reduction Reaction. *Chem. Soc. Rev.* **2010**, *39*, 2184–2202.
7. Mukerjee, S.; Srinivasan, S.; Soriaga, M. P.; McBreen, J. Effect of Preparation Conditions of Pt Alloys on Their Electronic, Structural, and Electrocatalytic Activities for Oxygen Reduction - XRD, XAS, and Electrochemical Studies. *J. Phys. Chem.* **1995**, *99*, 4577–4589.
8. Mukerjee, S.; Srinivasan, S.; Soriaga, M. P.; McBreen, J. Role of Structural and Electronic Properties of Pt and Pt Alloys on Electrocatalysis of Oxygen Reduction: An *in Situ* XANES and EXAFS Investigation. *J. Electrochem. Soc.* **1995**, *142*, 1409–1422.
9. Koh, S.; Strasser, P. Electrocatalysis on Bimetallic Surfaces: Modifying Catalytic Reactivity for Oxygen Reduction by

Voltammetric Surface Dealloying. *J. Am. Chem. Soc.* **2007**, *129*, 12624–12625.
10. Oezaslan, M.; Hasché, F.; Strasser, P. Pt-Based Core–Shell Catalyst Architectures for Oxygen Fuel Cell Electrodes. *J. Phys. Chem. Lett.* **2013**, *4*, 3273–3291.
11. Choi, S.-I.; Xie, S.; Shao, M.; Odell, J. H.; Lu, N.; Peng, H.-C.; Protsailo, L.; Guerrero, S.; Park, J.; Xia, X.; *et al*. Synthesis and Characterization of 9 nm Pt–Ni Octahedra with a Record High Activity of 3.3 A/mg_{Pt} for the Oxygen Reduction Reaction. *Nano Lett.* **2013**, *13*, 3420–3425.
12. Stamenkovic, V.; Mun, B. S.; Mayrhofer, K. J. J.; Ross, P. N.; Markovic, N. M.; Rossmeisl, J.; Greeley, J.; Nørskov, J. K. Changing the Activity of Electrocatalysts for Oxygen Reduction by Tuning the Surface Electronic Structure. *Angew. Chem., Int. Ed.* **2006**, *45*, 2897–2901.
13. Greeley, J.; Stephens, I. E. L.; Bondarenko, A. S.; Johansson, T. P.; Hansen, H. A.; Jaramillo, T. F.; Rossmeisl, J.; Chorkendorff, I.; Nørskov, J. K. Alloys of Platinum and Early Transition Metals as Oxygen Reduction Electrocatalysts. *Nat. Chem.* **2009**, *1*, 552–556.
14. Norskov, J. K.; Bligaard, T.; Rossmeisl, J.; Christensen, C. H. Towards the Computational Design of Solid Catalysts. *Nat. Chem.* **2009**, *1*, 37–46.
15. Mukerjee, S.; Srinivasan, S.; Soriaga, M. P.; McBreen, J. Role of Structural and Electronic Properties of Pt and Pt Alloys on Electrocatalysis of Oxygen Reduction. *J. Electrochem. Soc.* **1995**, *142*, 1409–1422.
16. Ruban, A.; Hammer, B.; Stoltze, P.; Skriver, H. L.; Nørskov, J. K. Surface Electronic Structure and Reactivity of Transition and Noble Metals. *J. Mol. Catal. A: Chem.* **1997**, *115*, 421–429.
17. Kitchin, J. R.; Nørskov, J. K.; Barteau, M. A.; Chen, J. G. Role of Strain and Ligand Effects in the Modification of the Electronic and Chemical Properties of Bimetallic Surfaces. *Phys. Rev. Lett.* **2004**, *93*, 156801.
18. Jia, Q.; Segre, C. U.; Ramaker, D.; Caldwell, K.; Trahan, M.; Mukerjee, S. Structure–Property–Activity Correlations of Pt-Bimetallic Nanoparticles: A Theoretical Study. *Electrochim. Acta* **2013**, *88*, 604–613.
19. Schlapka, A.; Lischka, M.; Groß, A.; Käsberger, U.; Jakob, P. Surface Strain *versus* Substrate Interaction in Heteroepitaxial Metal Layers: Pt on Ru(0001). *Phys. Rev. Lett.* **2003**, *91*, 016101.
20. Stamenkovic, V. R.; Mun, B. S.; Arenz, M.; Mayrhofer, K. J. J.; Lucas, C. A.; Wang, G.; Ross, P. N.; Markovic, N. M. Trends in Electrocatalysis on Extended and Nanoscale Pt-Bimetallic Alloy Surfaces. *Nat. Mater.* **2007**, *6*, 241–247.
21. Hammer, B.; Nørskov, J. K. In *Advances in Catalysis*; Bruce, C., Gates, H. K., Eds.; Academic Press, 2000; Vol. 45, pp 71–129.
22. Yu, T. H.; Hofmann, T.; Sha, Y.; Merinov, B. V.; Myers, D. J.; Heske, C.; Goddard, W. A. Finding Correlations of the Oxygen Reduction Reaction Activity of Transition Metal Catalysts with Parameters Obtained from Quantum Mechanics. *J. Phys. Chem. C* **2013**, *117*, 26598–26607.
23. Mukerjee, S.; Srinivasan, S. Enhanced Electrocatalysis of Oxygen Reduction on Platinum Alloys in Proton Exchange Membrane Fuel Cells. *J. Electroanal. Chem.* **1993**, *357*, 201–224.
24. Toda, T.; Igarashi, H.; Uchida, H.; Watanabe, M. Enhancement of the Electroreduction of Oxygen on Pt Alloys with Fe, Ni, and Co. *J. Electrochem. Soc.* **1999**, *146*, 3750–3756.
25. Oezaslan, M.; Strasser, P. Activity of Dealloyed $PtCo_3$ and $PtCu_3$ Nanoparticle Electrocatalyst for Oxygen Reduction Reaction in Polymer Electrolyte Membrane Fuel Cell. *J. Power Sources* **2011**, *196*, 5240–5249.
26. Hasché, F.; Oezaslan, M.; Strasser, P. Activity, Structure and Degradation of Dealloyed $PtNi_3$ Nanoparticle Electrocatalyst for the Oxygen Reduction Reaction in PEMFC. *J. Electrochem. Soc.* **2011**, *159*, B24–B33.
27. Mani, P.; Srivastava, R.; Strasser, P. Dealloyed Binary PtM_3 (M = Cu, Co, Ni) and Ternary $PtNi_3M$ (M = Cu, Co, Fe, Cr) Electrocatalysts for the Oxygen Reduction Reaction: Performance in Polymer Electrolyte Membrane Fuel Cells. *J. Power Sources* **2011**, *196*, 666–673.
28. Mani, P.; Srivastava, R.; Strasser, P. Dealloyed Pt–Cu Core–Shell Nanoparticle Electrocatalysts for Use in PEM Fuel Cell Cathodes. *J. Phys. Chem. C* **2008**, *112*, 2770–2778.
29. Chen, S.; Gasteiger, H. A.; Hayakawa, K.; Tada, T.; Shao-Horn, Y. Platinum–Alloy Cathode Catalyst Degradation in Proton Exchange Membrane Fuel Cells: Nanometer-Scale Compositional and Morphological Changes. *J. Electrochem. Soc.* **2010**, *157*, A82–A97.
30. Bonakdarpour, A.; Wenzel, J.; Stevens, D. A.; Sheng, S.; Monchesky, T. L.; Löbel, R.; Atanasoski, R. T.; Schmoeckel, A. K.; Vernstrom, G. D.; Debe, M. K.; *et al*. Studies of Transition Metal Dissolution from Combinatorially Sputtered, Nanostructured $Pt_{1-x}M_x$ (M = Fe, Ni; $0 < x < 1$) Electrocatalysts for PEM Fuel Cells. *J. Electrochem. Soc.* **2005**, *152*, A61–A72.
31. Strasser, P.; Koh, S.; Anniyev, T.; Greeley, J.; More, K.; Yu, C.; Liu, Z.; Kaya, S.; Nordlund, D.; Ogasawara, H.; *et al*. Lattice-Strain Control of the Activity in Dealloyed Core–Shell Fuel Cell Catalysts. *Nat. Chem.* **2010**, *2*, 454–460.
32. Cui, C.; Gan, L.; Neumann, M.; Heggen, M.; Roldan Cuenya, B.; Strasser, P. Carbon Monoxide-Assisted Size Confinement of Bimetallic Alloy Nanoparticles. *J. Am. Chem. Soc.* **2014**, *136*, 4813–4816.
33. Jia, Q.; Caldwell, K.; Strickland, K.; Ziegelbauer, J. M.; Liu, Z.; Yu, Z.; Ramaker, D. E.; Mukerjee, S. Improved Oxygen Reduction Activity and Durability of Dealloyed $PtCo_x$ Catalysts for Proton Exchange Membrane Fuel Cells: Strain, Ligand, and Particle Size Effects. *ACS Catal.* **2014**, 176–186.
34. Snyder, J.; McCue, I.; Livi, K.; Erlebacher, J. Structure/Processing/Properties Relationships in Nanoporous Nanoparticles As Applied to Catalysis of the Cathodic Oxygen Reduction Reaction. *J. Am. Chem. Soc.* **2012**, *134*, 8633–8645.
35. Kongkanand, A.; Wagner, F. *2014 Annual Merit Review, U.S. Department of Energy Hydrogen and Fuel Cells Program*, accessed July 30, **2014** http://www.hydrogen.energy.gov/pdfs/review14/fc087_kongkanand_2014_o.pdf.
36. Han, B.; Carlton, C. E.; Kongkanand, A.; Kukreja, R. S.; Theobald, B. R.; Gan, L.; O'Malley, R.; Strasser, P.; Wagner, F. T.; Shao-Horn, Y. Record Activity and Stability of Dealloyed Bimetallic Catalysts for Proton Exchange Membrane Fuel Cells. *Energy Environ. Sci.* **2015**, *8*, 258–266.
37. Jia, Q.; Caldwell, K.; Ziegelbauer, J. M.; Kongkanand, A.; Wagner, F. T.; Mukerjee, S.; Ramaker, D. E. The Role of OOH Binding Site and Pt Surface Structure on ORR Activities. *J. Electrochem. Soc.* **2014**, *161*, F1323–F1329.
38. Jia, Q.; Caldwell, K.; Ramaker, D. E.; Ziegelbauer, J. M.; Liu, Z.; Yu, Z.; Trahan, M.; Mukerjee, S. *In Situ* Spectroscopic Evidence for Ordered Core–Ultrathin Shell Pt_1Co_1 Nanoparticles with Enhanced Activity and Stability as Oxygen Reduction Electrocatalysts. *J. Phys. Chem. C* **2014**, *118*, 20496–20503.
39. Lai, F.-J.; Sarma, L. S.; Chou, H.-L.; Liu, D.-G.; Hsieh, C.-A.; Lee, J.-F.; Hwang, B.-J. Architecture of Bimetallic Pt_xCo_{1-x} Electrocatalysts for Oxygen Reduction Reaction As Investigated by X-ray Absorption Spectroscopy. *J. Phys. Chem. C* **2009**, *113*, 12674–12681.
40. Chen, S.; Sheng, W.; Yabuuchi, N.; Ferreira, P. J.; Allard, L. F.; Shao-Horn, Y. Origin of Oxygen Reduction Reaction Activity on "Pt_3Co" Nanoparticles: Atomically Resolved Chemical Compositions and Structures. *J. Phys. Chem. C* **2008**, *113*, 1109–1125.
41. Xu, Y.; Ruban, A. V.; Mavrikakis, M. Adsorption and Dissociation of O_2 on Pt–Co and Pt–Fe Alloys. *J. Am. Chem. Soc.* **2004**, *126*, 4717–4725.
42. Gauthier, Y.; Schmid, M.; Padovani, S.; Lundgren, E.; Buš, V.; Kresse, G.; Redinger, J.; Varga, P. Adsorption Sites and Ligand Effect for CO on an Alloy Surface: A Direct View. *Phys. Rev. Lett.* **2001**, *87*, 036103.
43. Yu, W.; Porosoff, M. D.; Chen, J. G. Review of Pt-Based Bimetallic Catalysis: From Model Surfaces to Supported Catalysts. *Chem. Rev.* **2012**, *112*, 5780–5817.
44. Tuaev, X.; Rudi, S.; Petkov, V.; Hoell, A.; Strasser, P. *In Situ* Study of Atomic Structure Transformations of Pt–Ni Nanoparticle Catalysts during Electrochemical Potential Cycling. *ACS Nano* **2013**, *7*, 5666–5674.

45. Koh, S.; Toney, M. F.; Strasser, P. Activity−Stability Relationships of Ordered and Disordered Alloy Phases of Pt_3Co Electrocatalysts for the Oxygen Reduction Reaction (ORR). *Electrochim. Acta* **2007**, *52*, 2765–2774.
46. Teliska, M.; O'Grady, W. E.; Ramaker, D. E. Determination of O and OH Adsorption Sites and Coverage *in Situ* on Pt Electrodes from Pt L_{23} X-ray Absorption Spectroscopy. *J. Phys. Chem. B* **2005**, *109*, 8076–8084.
47. Roth, C.; Benker, N.; Buhrmester, T.; Mazurek, M.; Loster, M.; Fuess, H.; Koningsberger, D. C.; Ramaker, D. E. Determination of O[H] and CO Coverage and Adsorption Sites on PtRu Electrodes in an Operating PEM Fuel Cell. *J. Am. Chem. Soc.* **2005**, *127*, 14607–14615.
48. Teliska, M.; O'Grady, W. E.; Ramaker, D. E. Determination of H Adsorption Sites on Pt/C Electrodes in $HClO_4$ from Pt L_{23} X-ray Absorption Spectroscopy. *J. Phys. Chem. B* **2004**, *108*, 2333–2344.
49. Ramaker, D. E.; Korovina, A.; Croze, V.; Melke, J.; Roth, C. Following ORR Intermediates Adsorbed on a Pt Cathode Catalyst during Break-in of a PEM Fuel Cell by in Operando X-ray Absorption Spectroscopy. *Phys. Chem. Chem. Phys.* **2014**, *16*, 13645–13653.
50. Ankudinov, A. L.; Ravel, B.; Rehr, J. J.; Conradson, S. D. Real-Space Multiple-Scattering Calculation and Interpretation of X-Ray Absorption Near-Edge Structure. *Phys. Rev. B* **1998**, *58*, 7565–7576.
51. Teliska, M.; Murthi, V. S.; Mukerjee, S.; Ramaker, D. E. Correlation of Water Activation, Surface Properties, and Oxygen Reduction Reactivity of Supported Pt−M/C Bimetallic Electrocatalysts Using XAS. *J. Electrochem. Soc.* **2005**, *152*, A2159–A2169.
52. Ramaker, D. E.; Koningsberger, D. C. Comment on "Effect of Hydrogen Adsorption on the X-Ray Absorption Spectra of Small Pt Clusters". *Phys. Rev. Lett.* **2002**, *89*, 139701.
53. Stamenkovic, V. R.; Fowler, B.; Mun, B. S.; Wang, G.; Ross, P. N.; Lucas, C. A.; Marković, N. M. Improved Oxygen Reduction Activity on $Pt_3Ni(111)$ *via* Increased Surface Site Availability. *Science* **2007**, *315*, 493–497.
54. Hwang, B.-J.; Sarma, L. S.; Chen, J.-M.; Chen, C.-H.; Shih, S.-C.; Wang, G.-R.; Liu, D.-G.; Lee, J.-F.; Tang, M.-T. Structural Models and Atomic Distribution of Bimetallic Nanoparticles as Investigated by X-ray Absorption Spectroscopy. *J. Am. Chem. Soc.* **2005**, *127*, 11140–11145.
55. Yang, R.; Strasser, P.; Toney, M. F. Dealloying of Cu_3Pt (111) Studied by Surface X-ray Scattering. *J. Phys. Chem. C* **2011**, *115*, 9074–9080.
56. Alayoglu, S.; Zavalij, P.; Eichhorn, B.; Wang, Q.; Frenkel, A. I.; Chupas, P. Structural and Architectural Evaluation of Bimetallic Nanoparticles: A Case Study of Pt−Ru Core−Shell and Alloy Nanoparticles. *ACS Nano* **2009**, *3*, 3127–3137.
57. Erlebacher, J.; Aziz, M. J.; Karma, A.; Dimitrov, N.; Sieradzki, K. Evolution of Nanoporosity in Dealloying. *Nature* **2001**, *410*, 450–453.
58. Mukerjee, S.; McBreen, J. Effect of Particle Size on the Electrocatalysis by Carbon-Supported Pt Electrocatalysts: An *in Situ* XAS Investigation. *J. Electroanal. Chem.* **1998**, *448*, 163–171.
59. Lei, Y.; Zhao, H.; Rivas, R. D.; Lee, S.; Liu, B.; Lu, J.; Stach, E.; Winans, R. E.; Chapman, K. W.; Greeley, J. P.; *et al.* Adsorbate-Induced Structural Changes in 1−3 nm Platinum Nanoparticles. *J. Am. Chem. Soc.* **2014**, *136*, 9320–9326.
60. Hernandez-Fernandez, P.; Masini, F.; McCarthy, D. N.; Strebel, C. E.; Friebel, D.; Deiana, D.; Malacrida, P.; Nierhoff, A.; Bodin, A.; Wise, A. M.; *et al.* Mass-Selected Nanoparticles of Pt_xY as Model Catalysts for Oxygen Electroreduction. *Nat. Chem.* **2014**, *6*, 732–738.
61. Shao, M.; Peles, A.; Shoemaker, K. Electrocatalysis on Platinum Nanoparticles: Particle Size Effect on Oxygen Reduction Reaction Activity. *Nano Lett.* **2011**, *11*, 3714–3719.
62. Antolini, E.; Salgado, J. R. C.; Giz, M. J.; Gonzalez, E. R. Effects of Geometric and Electronic Factors on ORR Activity of Carbon Supported Pt−Co Electrocatalysts in PEM Fuel Cells. *Int. J. Hydrogen Energy* **2005**, *30*, 1213–1220.
63. Liu, Y.; Mustain, W. E. High Stability, High Activity Pt/ITO Oxygen Reduction Electrocatalysts. *J. Am. Chem. Soc.* **2012**, *135*, 530–533.
64. Cui, C.; Gan, L.; Heggen, M.; Rudi, S.; Strasser, P. Compositional Segregation in Shaped Pt Alloy Nanoparticles and Their Structural Behaviour during Electrocatalysis. *Nat. Mater.* **2013**, *12*, 765–771.
65. Wang, C.; Daimon, H.; Onodera, T.; Koda, T.; Sun, S. A General Approach to the Size- and Shape-Controlled Synthesis of Platinum Nanoparticles and Their Catalytic Reduction of Oxygen. *Angew. Chem.* **2008**, *120*, 3644–3647.
66. Gan, L.; Heggen, M.; O'Malley, R.; Theobald, B.; Strasser, P. Understanding and Controlling Nanoporosity Formation for Improving the Stability of Bimetallic Fuel Cell Catalysts. *Nano Lett.* **2013**, *13*, 1131–1138.
67. Arruda, T. M.; Shyam, B.; Lawton, J. S.; Ramaswamy, N.; Budil, D. E.; Ramaker, D. E.; Mukerjee, S. Fundamental Aspects of Spontaneous Cathodic Deposition of Ru onto Pt/C Electrocatalysts and Membranes under Direct Methanol Fuel Cell Operating Conditions: An *in Situ* X-ray Absorption Spectroscopy and Electron Spin Resonance Study. *J. Phys. Chem. C* **2009**, *114*, 1028–1040.
68. Newville, M. IFEFFIT: Interactive XAFS Analysis and FEFF Fitting. *J. Synchrotron Radiat.* **2001**, *8*, 322–324.
69. Ravel, B.; Gallagher, K. Atomic Structure and the Magnetic Properties of Zr-Doped Sm_2Co_{17}. *Phys. Scr.* **2005**, *2005*, 606.
70. Newville, M.; Limacrvincedilscaron, P.; Yacoby, Y.; Rehr, J. J.; Stern, E. A. Near-Edge X-Ray Absorption Fine Structure of Pb: A Comparison of Theory and Experiment. *Phys. Rev. B* **1993**, *47*, 14126.
71. Jia, Q.; Ramaker, D. E.; Ziegelbauer, J. M.; Ramaswamy, N.; Halder, A.; Mukerjee, S. Fundamental Aspects of ad-Metal Dissolution and Contamination in Low and Medium Temperature Fuel Cell Electrocatalysis: A Cu Based Case Study Using *in Situ* Electrochemical X-ray Absorption Spectroscopy. *J. Phys. Chem. C* **2013**, *117*, 4585–4596.